

Bayesian optimization with Gaussian process surrogate model for source localization

William F. Jenkins II,^{a)}  Peter Gerstoft,  and Yongsung Park 

Scripps Institution of Oceanography, University of California San Diego, La Jolla, California 92093, USA

ABSTRACT:

Source localization with a geoacoustic model requires optimizing the model over a parameter space of range and depth with the objective of matching a predicted sound field to a field measured on an array. We propose a sample-efficient sequential Bayesian optimization strategy that models the objective function as a Gaussian process (GP) surrogate model conditioned on observed data. Using the mean and covariance functions of the GP, a heuristic acquisition function proposes a candidate in parameter space to sample, balancing exploitation (sampling around the best observed objective function value) and exploration (sampling in regions of high variance in the GP). The candidate sample is evaluated, and the GP conditioned on the updated data. Optimization proceeds sequentially until a fixed budget of evaluations is expended. We demonstrate source localization for a shallow-water waveguide using Monte Carlo simulations and experimental data from an acoustic source tow. Compared to grid search and quasi-random sampling strategies, simulations and experimental results indicate the Bayesian optimization strategy converges on optimal solutions rapidly. © 2023 Acoustical Society of America. <https://doi.org/10.1121/10.0020839>

(Received 30 May 2023; revised 25 July 2023; accepted 16 August 2023; published online 7 September 2023)

[Editor: Zoi-Heleni Michalopoulou]

Pages: 1459–1470

I. INTRODUCTION

Sound propagation in the ocean depends on the physical properties and geometry of the media through which it travels. Using numerical techniques and physical theory, underwater acoustic propagation models predict sound fields in complex environments, enabling estimation of the ocean environment. However, since these models cannot be explicitly inverted, ocean parameters are estimated by sampling parameter space and evaluating samples with a forward model. Forward model predictions are then compared to observed data, with the quality of the prediction given by the correlation—i.e., the match between the predicted and observed data.

In this study, we present a strategy which casts the inverse problem as a sequential Bayesian optimization problem. Rather than directly optimizing a computationally expensive objective function which could have a complicated structure with many local minima and maxima, a Gaussian process (GP) is fit to the observed data and acts as a surrogate model of the objective function surface. A GP surrogate model is convenient as it provides a tractable approach to modeling the posterior distribution of a function,¹ and has been successfully used to predict sound fields and improve acoustic source direction of arrival estimation, localization, and geoacoustic inversion.^{2–5} More broadly, GP regression is also referred to as kriging and has been used extensively in the geosciences and other fields.⁶

The GP model consists of a mean function and covariance function that describe the uncertainty in the objective function: regions which have been sampled exhibit lower

uncertainty, while those which remain unexplored exhibit higher uncertainty.^{1,7} Once the GP is fit to the data, a sequential Bayesian framework is applied in which a candidate sample is heuristically proposed by an acquisition function based on the first and second moments of the GP model.^{8,9} The candidate sample is evaluated and the GP model is updated with the new evaluation. This sequential optimization repeats until a maximum budget of objective function evaluations, or trials, is expended.

The design of the acquisition function determines how efficiently the sequential optimization strategy performs.¹⁰ Key to performance of acquisition functions is their ability to balance exploration, sampling in regions of high uncertainty in the GP model, with exploitation, sampling near the best observed value. Conventional acquisition functions derive an analytical function from the mean and covariance functions of the GP model posterior. For example, the upper confidence bound acquisition function proposes a candidate sample where the uncertainty in the GP posterior is greatest.¹¹ Others, such as the probability of improvement (PI) and expected improvement (EI) acquisition functions, take into account both the uncertainty and mean of the GP posterior, offering an enhanced balance between exploration and exploitation.¹⁰ Recent developments have introduced multi-point versions of conventional acquisition functions, in which the acquisition function suggests multiple candidate samples within each iteration of the sequential optimization.^{12–15} Candidates are suggested through a quasi-Monte Carlo generation scheme or a sequential greedy optimization scheme and tend to outperform conventional acquisition functions in synthetic experiments.

^{a)}Email: wjenkins@ucsd.edu

This study demonstrates acoustic source localization in a shallow waveguide using sequential Bayesian optimization with a GP surrogate model. Performance of two acquisition functions is compared to conventional sampling techniques using both acoustic simulations and data from an acoustic source tow experiment. The paper is organized as follows: Sec. II summarizes alternative and previous methods; Sec. III describes the optimization problem and Bayesian optimization algorithm; Sec. IV presents simulation and experimental results for source localization in a shallow-water waveguide; and Sec. V contains remarks on implementation considerations. Code used for this study is available online.¹⁶

II. ALTERNATIVE STRATEGIES FOR OPTIMIZATION

Numerous strategies for sampling the parameter space are available. A simple but computationally expensive strategy is matched field processing (MFP), a well known application of grid search typically conducted over source range, depth, and other geoacoustic parameters, such as ocean bottom composition.¹⁷ A challenge with MFP is extending the parameter search space to more parameters can make the computational cost of the optimization untenable, since the cost of grid search scales exponentially with parameter dimension.

Randomly sampling parameter space can accumulate sufficient evaluations to estimate the global optimum but is vulnerable to repeatedly sampling from the same region or missing the global optimum altogether.¹⁸ Quasi-random techniques achieve lower discrepancies, ensuring a more even distribution of samples over the parameter space. A popular quasi-random approach uses a Sobol sequence to generate points in high-dimensional space with low discrepancy,^{19–21} and has been used for global sensitivity analysis in geoacoustic inversion²² and in wind turbine noise uncertainty quantification.²³

Grid search, random sampling, and Sobol sampling make no use of the information about the objective function after a sample is evaluated. The gradient of an objective is an example of information that can guide the search. Cases where information about the gradient of the objective is known are often solved with methods such as gradient descent or the Broyden-Fletcher-Goldfarb-Shanno (BFGS) family of optimizers.²⁴ However, for source localization the ambiguity surface is non-convex and characterized by local optima due to interference patterns. Furthermore, estimating the gradient can be computationally expensive, requiring multiple forward model evaluations. While beamforming methods such as MUSIC²⁵ and sparse Bayesian learning (SBL)^{26–29} improve resolution and reduce ambiguities in the objective, such methods are still evaluated at grid points and alleviate neither computational cost nor the challenge of non-convexity. Methods such as gradient descent and BFGS are therefore ineffective, as their success depends on the initialization point and might converge on a local optimum.

Recent advances in machine learning have enabled approaches to non-convex optimization such as matrix

completion,^{30,31} as well as data-driven approaches to acoustic parameter estimation using neural networks and deep learning.^{32–35} Traditional time-difference-of-arrival and bearing-of-arrival localization methods continue to be enhanced through advances in optimization techniques.³⁶ In this study, we focus on Bayesian optimization strategies, which use observed values of the objective function to guide the search for the globally optimal solution.

Existing Bayesian approaches to geoacoustic parameter estimation largely rely on treating the ambiguity surface as a posterior distribution over the parameter space and using Monte Carlo sampling to directly estimate the moments of the posterior. A popular approach to geoacoustic parameter estimation uses Markov chain Monte Carlo (MCMC) optimization through genetic algorithms and simulated annealing, with Gibbs sampling providing unbiased moment estimates of the posterior distribution.^{37–41} While simulated annealing and genetic algorithms offer practical and robust methods for global optimization, they take many iterations to converge and require hyperparameter tuning.^{37,42–44} Numerous advancements in MCMC techniques have since been demonstrated, including trans-dimensional techniques which treat the number of parameters to be estimated as an unknown quantity which must be estimated.^{45–47}

To leverage the benefits of local optimization techniques with the global search capabilities of MCMC, hybrid methods combining genetic algorithms with the Gauss-Newton and simplex algorithms have been demonstrated in geoacoustic inversion problems, leading to faster convergence and improved estimation.^{48,49} In a conceptually similar vein, our approach uses quasi-random sampling to initialize sequential Bayesian optimization, hastening convergence and improving optimization performance. Figure 1 demonstrates the advantage of sequential Bayesian optimization over grid search and Sobol sampling in an acoustic localization parameter space. Given 144 trials, grid search [Fig. 1(a)] and Sobol sequence sampling [Fig. 1(b)] are unable to resolve the global optimum, whereas Bayesian optimization [Fig. 1(c)] initialized with 128 samples of a Sobol sequence converges on the global optimum within the allotted trial budget.

III. BAYESIAN OPTIMIZATION FRAMEWORK

A. Objective function definition

Consider an array with M hydrophones that measures an acoustic pressure field $\mathbf{d} \in \mathbb{C}^M$ at a single frequency. In the forward problem, the field measured at the receiver array is described by an acoustic propagation model $G(\mathbf{x})$,

$$\mathbf{d} = G(\mathbf{x}), \quad (1)$$

where the parameterization $\mathbf{x} \in \mathcal{X}^D$ describes the acoustic source location and geoacoustic properties of the propagation environment, and \mathcal{X}^D is a domain bounded by finite bounds on each of the D parameters within \mathbf{x} . Our task is to solve the inverse problem: given the model G , we seek to

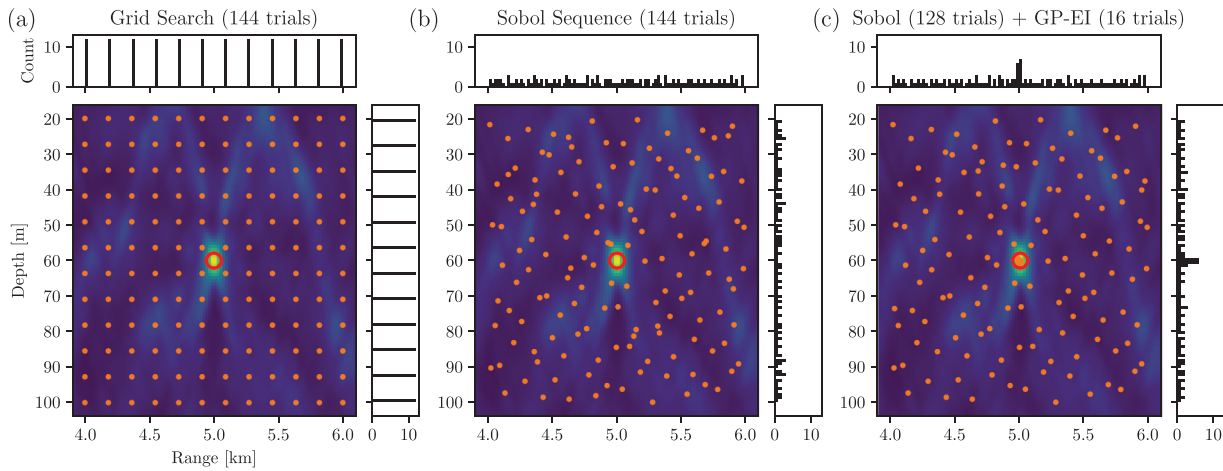


FIG. 1. (Color online) True source location (red circle) and sample locations (orange) for 144 objective function evaluations (trials) using (a) a 12×12 grid search, (b) Sobol sequence sampling, and (c) Bayesian optimization using a Gaussian process with expected improvement acquisition function (GP-EI). Marginal sample histograms are along the axes.

find an estimate $\hat{\mathbf{x}}$ of the true parameters \mathbf{x}_{true} that produce an observed pressure field $\mathbf{d}_{\text{obs}} \in \mathbb{C}^M$.

To find $\hat{\mathbf{x}}$, the parameter space \mathcal{X} is sampled and each sample \mathbf{x} is evaluated using Eq. (1), producing replica acoustic pressure fields $\mathbf{d}(\mathbf{x}) \in \mathbb{C}^M$. Relying on the interference patterns that occur due to acoustic propagation in an ocean waveguide, $\hat{\mathbf{x}}$ is obtained by finding the parameters that yield a predicted replica field which most closely matches the actual field. On every evaluation of $G(\mathbf{x})$, the coherence between the replica field \mathbf{d} and the observed field \mathbf{d}_{obs} is computed using the Bartlett power

$$f(\mathbf{x}) = |\mathbf{w}(\mathbf{x})^H \check{\mathbf{d}}|^2, \quad (2)$$

where $\mathbf{w}(\mathbf{x})$ is the normalized replica field

$$\mathbf{w}(\mathbf{x}) = \mathbf{d}(\mathbf{x}) / \|\mathbf{d}(\mathbf{x})\| \quad (3)$$

and $\check{\mathbf{d}}$ is the normalized observed field

$$\check{\mathbf{d}} = \mathbf{d}_{\text{obs}} / \|\mathbf{d}_{\text{obs}}\| \quad (4)$$

to ensure Eq. (2) is normalized to the interval $[0, 1]$.

In this localization study, only source range R_{src} and source depth z_{src} are estimated ($\mathbf{x} = [R_{\text{src}}, z_{\text{src}}]^T$); all other geoacoustic properties of the propagation environment are known. We define a multi-frequency objective function by incoherently averaging Eq. (2) computed over each frequency in $\Omega = \{\omega_1, \omega_2, \dots\}$,^{50,51}

$$f(\mathbf{x}) = \frac{1}{|\Omega|} \sum_{i=1}^{|\Omega|} f(\mathbf{x} | \omega_i). \quad (5)$$

Every evaluation of Eq. (5) requires an evaluation of the propagation model at $|\Omega|$ frequencies. Evaluating Eq. (5) over \mathcal{X} produces an ambiguity surface whose global maximum occurs where the replica and received pressure fields across all frequencies are most coherent, giving

$$\hat{\mathbf{x}} = \arg \max_{\mathbf{x} \in \mathcal{X}} [f(\mathbf{x})]. \quad (6)$$

Using the multi-frequency ambiguity surface of Eq. (5) to compute Eq. (6) improves optimization performance by averaging out frequency-dependent ambiguities, suppressing sidelobes, and smoothing the ambiguity surface, all of which improve the likelihood of converging to the global optimum.

B. Gaussian process surrogate model

Formally, a GP is a collection of random variables, any finite number of which have a joint Gaussian distribution.^{1,7} Here, we follow the derivations of Ref. 7. Consider N samples from the D -dimensional parameter space $\mathbf{X} = [\mathbf{x}_1, \dots, \mathbf{x}_N] \in \mathcal{X}^{D \times N}$. Given a real process $\mathbf{f} = [f(\mathbf{x}_1), \dots, f(\mathbf{x}_N)]^T$ as in Eq. (5), a GP is described completely by two functions: a mean function,

$$\boldsymbol{\mu} = \mathbb{E}[\mathbf{f}] = [\mu(\mathbf{x}_1), \dots, \mu(\mathbf{x}_N)]^T \in \mathbb{R}^N, \quad (7)$$

where $\mu(\mathbf{x}_n)$ is the mean at \mathbf{x}_n and a covariance function,

$$\Sigma_{ij} = \mathbb{E}[(f(\mathbf{x}_i) - \mu(\mathbf{x}_i))(f(\mathbf{x}_j) - \mu(\mathbf{x}_j))] \quad (8)$$

$$= \mathcal{K}(\mathbf{x}_i, \mathbf{x}_j) \in \mathbb{R}^{N \times N}, \quad (9)$$

where $\mathcal{K}(\mathbf{x}_i, \mathbf{x}_j)$ is a kernel function measuring the similarity between points \mathbf{x}_i and \mathbf{x}_j . The GP is summarized as

$$\mathbf{f} \sim \mathcal{GP}(\boldsymbol{\mu}, \Sigma). \quad (10)$$

A GP has observations at sampled parameters comprising the set

$$\mathcal{D} = \{(\mathbf{x}_n, y_n), n = 1 : N\} = \{\mathbf{X}, \mathbf{y}\}, \quad \mathbf{y} \in \mathbb{R}^N. \quad (11)$$

Though observations of the ambiguity surface are deterministic (in contrast with the data \mathbf{d} used to generate the ambiguity surface), to improve numerical stability in subsequent

matrix inversions, we allow for additive Gaussian noise $\epsilon_n \sim \mathcal{N}(0, \sigma_y^2)$ in the observations on the order of 10^{-8} ,

$$y_n = f(\mathbf{x}_n) + \epsilon_n. \quad (12)$$

Interpolation with a GP is performed by predicting a set of N^* unobserved outputs \mathbf{f}_* at inputs $\mathbf{X}_{*,D \times N^*} = [\mathbf{x}_1^*, \dots, \mathbf{x}_{N^*}^*]$. The joint distribution of the observed process \mathbf{y} and the predictive distribution \mathbf{f}_* is [Ref. 7, Eq. (17.33), Ref. 1, Eq. (2.21)]

$$p(\mathbf{y}, \mathbf{f}_* | \mathbf{X}, \mathbf{X}_*) = \begin{bmatrix} \mathbf{y} \\ \mathbf{f}_* \end{bmatrix} = \mathcal{N}\left(\begin{bmatrix} \boldsymbol{\mu}_X \\ \boldsymbol{\mu}_* \end{bmatrix}, \begin{bmatrix} \hat{\mathbf{K}}_{X,X} & \mathbf{K}_{X,*} \\ \mathbf{K}_{X,*}^\top & \mathbf{K}_{*,*} \end{bmatrix}\right), \quad (13)$$

where $\boldsymbol{\mu}_X$ and $\boldsymbol{\mu}_*$ are the mean functions at \mathbf{X} and \mathbf{X}_* , and

$$\hat{\mathbf{K}}_{X,X} = \mathbf{K}_{X,X} + \sigma_y^2 \mathbf{I} = \mathcal{K}(\mathbf{X}, \mathbf{X})_{N \times N} + \sigma_y^2 \mathbf{I}, \quad (14)$$

$$\mathbf{K}_{X,*} = \mathcal{K}(\mathbf{X}, \mathbf{X}_*)_{N \times N_*}, \quad (15)$$

$$\mathbf{K}_{*,*} = \mathcal{K}(\mathbf{X}_*, \mathbf{X}_*)_{N_* \times N_*}, \quad (16)$$

where \mathcal{K} is a kernel function defined in Sec. III B 1. The posterior distribution is obtained by conditioning the GP on the new observations [Ref. 7, Eq. (17.34), Ref. 1, Eq. (2.22)],

$$p(\mathbf{f}_* | \mathcal{D}, \mathbf{X}_*) = \mathcal{N}(\mathbf{f}_* | \boldsymbol{\mu}_{*|X}, \boldsymbol{\Sigma}_{*|X}), \quad (17)$$

$$\boldsymbol{\mu}_{*|X} = \boldsymbol{\mu}_* + \mathbf{K}_{X,*}^\top \hat{\mathbf{K}}_{X,X}^{-1} (\mathbf{y} - \boldsymbol{\mu}_X), \quad (18)$$

$$\boldsymbol{\Sigma}_{*|X} = \mathbf{K}_{*,*} - \mathbf{K}_{X,*}^\top \hat{\mathbf{K}}_{X,X}^{-1} \mathbf{K}_{X,*}. \quad (19)$$

1. Kernel function

An important component of the GP surrogate model is the kernel function [Eq. (9)], which measures the similarity between two points so that as \mathbf{x}_i and \mathbf{x}_j become more similar, so do their outputs $f(\mathbf{x}_i)$ and $f(\mathbf{x}_j)$. This relationship is critical to predicting unobserved data points as in Eqs. (13)–(19). We use a kernel which is (1) positive definite and (2) stationary with real-valued inputs, i.e.,

$$\mathcal{K}(\mathbf{x}_i, \mathbf{x}_j) = \mathcal{K}(\mathbf{r}), \quad \mathbf{r} = \mathbf{x}_i - \mathbf{x}_j. \quad (20)$$

Specifically, we adopt the Matern kernel^{1,7} as it captures variability in length scales and allows for roughness in its output, characteristics which are useful in approximating a non-convex ambiguity surface. The Matern kernel is given in one dimension by

$$\mathcal{K}(r; \nu, l) = \sigma_y^2 \frac{2^{1-\nu}}{\Gamma(\nu)} \left(\frac{\sqrt{2\nu r}}{l} \right)^\nu K_\nu \left(\frac{\sqrt{2\nu r}}{l} \right), \quad (21)$$

where K_ν is the modified Bessel function. $\sigma_y \in \mathbb{R}$, $l \in \mathbb{R}$, and $\nu \in \{1/2, 3/2, 5/2, \dots\}$ are hyperparameters, with σ_y^2 estimating the noise variance of the GP, l controlling the length scale, and ν controlling the roughness of the kernel output. Higher

values of ν result in smoother outputs, with $\nu \rightarrow \infty$ giving the squared exponential kernel; we adopt the typical choice of $\nu = 5/2$ [Ref. 7, Eq. (17.13), Ref. 1, Eq. (4.17)]. Using automatic relevance determination (ARD), characteristic length scales are estimated for each dimension by modifying Eq. (21) to [Ref. 52, Sec. 1.2.3, Ref. 1, Sec. 5.1, Ref. 7, Eq. (17.8)]

$$\mathcal{K}\left(\mathbf{r}; \frac{5}{2}, \mathbf{l}\right) = \sigma_y^2 \prod_{d=1}^D \left(1 + \frac{\sqrt{5}r_d}{l_d} + \frac{5r_d^2}{3l_d^2} \right) \exp\left(-\frac{\sqrt{5}r_d}{l_d}\right), \quad (22)$$

where r_d is the distance between points \mathbf{x}_1 and \mathbf{x}_2 along dimension d , and characteristic length scales for each dimension are given by $\mathbf{l} = [l_1, l_2, \dots, l_D]$.

2. Kernel hyperparameter optimization

The Matern kernel function contains hyperparameters $\boldsymbol{\theta} = [\sigma_y^2, \mathbf{l}]$ which must be optimized for the GP surrogate model to appropriately reflect the data.^{1,7} Kernel function fitting occurs after new samples are drawn but before the predictive distribution is computed in Eq. (13) and is efficiently solved with an empirical-Bayes approach.⁷ To optimize $\boldsymbol{\theta}$, the marginal likelihood is maximized [Ref. 7, Eq. (17.51)],

$$p(\mathbf{y} | \mathbf{X}, \boldsymbol{\theta}) = \int p(\mathbf{y} | \mathbf{f}, \mathbf{X}) p(\mathbf{f} | \mathbf{X}, \boldsymbol{\theta}) d\mathbf{f}, \quad (23)$$

where treating $\boldsymbol{\theta}$ as implicit in $\hat{\mathbf{K}}_{X,X}$,

$$p(\mathbf{f} | \mathbf{X}) = \mathcal{N}(\mathbf{f} | \boldsymbol{\mu}_X, \hat{\mathbf{K}}_{X,X}), \quad (24)$$

$$p(\mathbf{y} | \mathbf{f}) = \prod_{n=1}^N \mathcal{N}(y_n | f_n, \sigma_y^2). \quad (25)$$

The log marginal likelihood and its derivative are then [Ref. 53, Eq. (18.74), Ref. 7, Eq. (17.52)]

$$\begin{aligned} L &= \log p(\mathbf{y} | \mathbf{X}, \boldsymbol{\theta}) \\ &= \log \mathcal{N}(\mathbf{y} | \boldsymbol{\mu}_X, \hat{\mathbf{K}}_{X,X}) \\ &= -\frac{1}{2} (\mathbf{y} - \boldsymbol{\mu}_X)^\top \hat{\mathbf{K}}_{X,X}^{-1} (\mathbf{y} - \boldsymbol{\mu}_X) \\ &\quad - \frac{1}{2} \log |\hat{\mathbf{K}}_{X,X}| - \frac{N}{2} \log (2\pi), \end{aligned} \quad (26)$$

$$\frac{\partial L}{\partial \theta_j} = \frac{1}{2} \text{tr} \left[(\boldsymbol{\alpha} \boldsymbol{\alpha}^\top - \hat{\mathbf{K}}_{X,X}) \frac{\partial \hat{\mathbf{K}}_{X,X}}{\partial \theta_j} \right], \quad (27)$$

where $\boldsymbol{\alpha} = \hat{\mathbf{K}}_{X,X}^{-1} (\mathbf{y} - \boldsymbol{\mu}_X)$. In contrast to the ambiguity surface, since Eq. (26) is smoothly varying with few optima, hyperparameter optimization is performed with the bounded Limited-memory BFGS (L-BFGS-B) algorithm, a quasi-Newtonian method that finds a minimizing solution given a starting point $\mathbf{x} \in \mathcal{X}$ and a smooth objective function.^{54,55} L-BFGS-B terminates either by comparing Eq. (26) between iterations k and $k+1$ according to the condition

$$\frac{L^k - L^{k+1}}{\max(|L^k|, |L^{k+1}|, 1)} \leq 10^7 \varepsilon, \quad (28)$$

where $\varepsilon \sim \mathcal{O}(10^{-16})$ is the machine precision; or when Eq. (27) projected onto the feasible parameter space \mathcal{X} (denoted by the Proj operator) meets the condition

$$\max_{j \in \{1, \dots, D\}} \left| \text{Proj} \left(\frac{\partial L}{\partial \theta_j} \right) \right| \leq 10^{-5}. \quad (29)$$

To improve convergence in hyperparameter optimization, prior distributions are placed over the kernel hyperparameters from which starting points for L-BFGS-B are selected. For computational stability, parameters are normalized to $[0, 1]$ and observations standardized to zero mean and unit variance before fitting the GP. For length scales \mathbf{l} , a Gamma distribution [Ref. 7, Sec. 2.7.5] is adopted with shape $a = 3$ and rate $b = 6$, yielding a distribution with a mean of 0.5. We find this is a reasonable choice for the transformed parameter space as the prior encourages samples consistent with expected correlation length scales given the source frequencies and geometry of the shallow waveguide.⁵⁶ For the noise variance σ_y^2 , a Gamma distribution with shape $a = 2$ and rate $b = 0.15$ is adopted.

Examples of Matern kernel hyperparameter optimization are shown in Fig. 2 for a one-dimensional GP regression on a broadband ambiguity surface computed over source range. Figure 2(a) shows the negative log likelihood [Eq. (26)] over the $\boldsymbol{\theta} = [\sigma_y^2, l]$ hyperparameters. The model fits indicated by the white stars correspond to the optimal GP regression in Fig. 2(b) and a suboptimal GP regression in Fig. 2(c) whose noise variance and length scale are too large.

C. Acquisition functions

Acquisition functions provide a heuristic which guides the sequential sampling strategy. Since the dataset \mathcal{D} grows with every iteration, and to differentiate from the sample index n , we introduce a trial index t to denote sequential

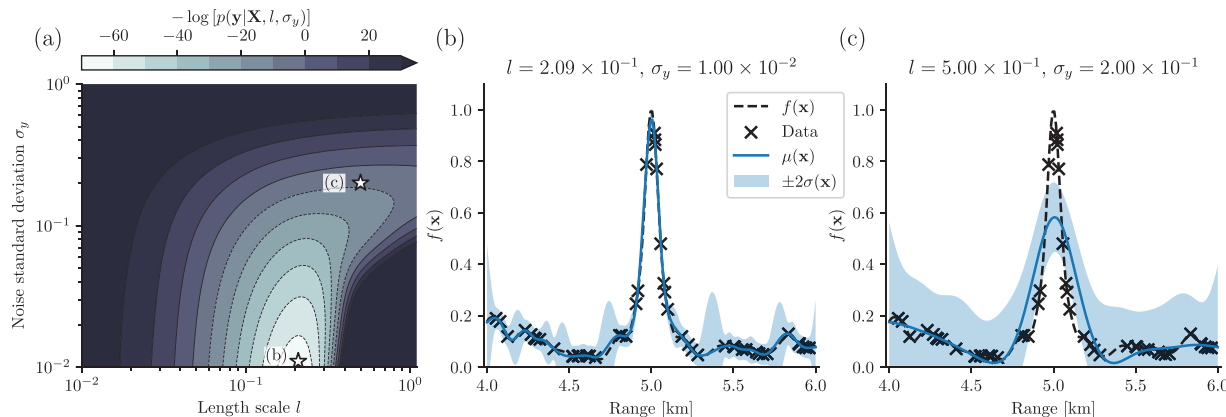


FIG. 2. (Color online) Hyperparameter optimization for Gaussian process (GP) regression on a one-dimensional broadband ambiguity surface computed over source range. (a) Negative log-likelihood of a Matern kernel function vs the noise standard deviation and length scale hyperparameters. Labeled stars indicate the resulting GP regression for (b) the optimal fit and (c) a suboptimal fit.

operations. At every trial t , a new sample is drawn, evaluated, and appended to the previously evaluated data by

$$\mathcal{D}|_t = \mathcal{D}|_{t-1} \cup \{(\mathbf{x}_t, f(\mathbf{x}_t))\}. \quad (30)$$

To select the next point in parameter space \mathbf{x}_t which will be evaluated, an acquisition function α takes the GP predictive posterior distribution as its input and returns a proposed candidate for the next trial by

$$\mathbf{x}_t = \arg \max_{\mathbf{x}} \alpha(f(\mathbf{x})). \quad (31)$$

Numerous algorithmic implementations are available to compute α ; here we evaluate two heuristics defined by the expected improvement over previous observations. Given a set of observations \mathcal{D} , let f' be the largest observed value of \mathbf{f} and the improvement over f' at any point \mathbf{x} be defined as¹⁰

$$I(\mathbf{x}) = \max(f(\mathbf{x}) - f', 0), \quad (32)$$

noting that $I \geq 0$. I is a random variable since the uncertainty of the objective function is encoded in $\mathbf{f} \sim \mathcal{N}(\mu, \Sigma)$.

The covariance function Σ of the posterior distribution \mathbf{f} is assumed diagonal and the variance $\sigma^2(\mathbf{x})$ is

$$\Sigma \approx \text{diag}[\sigma^2(\mathbf{x}_1), \dots, \sigma^2(\mathbf{x}_N)]. \quad (33)$$

Using $\sigma(\mathbf{x})$, we use the re-parameterization trick to rewrite the posterior distribution as

$$f(\mathbf{x}) = \mu(\mathbf{x}) + \sigma(\mathbf{x})z. \quad (34)$$

The improvement as defined in Eq. (32) is then rewritten

$$I(\mathbf{x}) = \max(\mu(\mathbf{x}) + \sigma(\mathbf{x})z - f', 0). \quad (35)$$

1. Expected improvement (EI)

Expected improvement (EI) gives the expected magnitude in improvement over the best previously observed evaluation of the objective function.¹⁰ Defining z_0 as

$$z_0(\mathbf{x}) = \frac{f' - \mu(\mathbf{x})}{\sigma(\mathbf{x})}. \quad (36)$$

EI is computed by evaluating the upper side of the cumulative distribution function $\Phi(z)$ and the normal probability distribution function $\varphi(z)$,

$$\begin{aligned} EI(\mathbf{x}) &= \mathbb{E}[I(\mathbf{x})] \\ &= \mathbb{E}[\max(\mu(\mathbf{x}) + \sigma(\mathbf{x})z - f', 0)] \\ &= (\mu(\mathbf{x}) - f') (1 - \Phi(z_0(\mathbf{x}))) + \sigma(\mathbf{x})\varphi(z_0(\mathbf{x})). \end{aligned} \quad (37)$$

EI is increased either by reduction of the mean $\mu(\mathbf{x})$ (exploitation) or the variance $\sigma(\mathbf{x})$ (exploration). From Eq. (31), the point \mathbf{x}_t that maximizes Eq. (37) is selected for evaluation in the subsequent trial.

The EI acquisition function assumes a noise free measurement of f' , but from Eq. (12), a small amount of noise in the objective function evaluation is expected. To avoid slow or incorrect convergence, we use an implementation of EI which accounts for a noisy objective function.⁵⁷

2. q-expected improvement (qEI)

Recent work^{12–15} extends improvement-based acquisition functions by implementing parallel evaluations of the acquisition function. One such implementation, quasi-Monte Carlo EI (q-Expected Improvement, or qEI), evaluates a batch of q random samples $\mathbf{X} = [\mathbf{x}_1, \dots, \mathbf{x}_q] \in \mathcal{X}$ with

ALGORITHM 1. Optimization of analytic (part A, EI, and PI) and quasi-Monte Carlo (part B, qEI) acquisition functions.

Input: Parameter domain \mathcal{X} , acquisition function α , number of raw samples N_{raw} , number of restarts N_{restart}

Output: Next sample point \mathbf{x}_t or points \mathbf{X}_t

Initialization:

1. $\mathbf{x}_t \leftarrow \mathbf{0}$, $\tilde{\alpha} \leftarrow 0$
2. $\tilde{\mathbf{X}} \leftarrow$ Draw N_{raw} i.i.d. samples from \mathcal{X}
3. $\tilde{\alpha} \leftarrow \alpha(\tilde{\mathbf{X}})$ [Eq. (42)]
4. $\mathbf{z} \leftarrow \frac{\tilde{\alpha} - \text{mean}(\tilde{\alpha})}{\text{std}(\tilde{\alpha})}$ [Eq. (43)]

Part A: Expected Improvement

5. **for** $i = 1$ to N_{restart} **do**
6. $\mathbf{x} \leftarrow$ Draw sample from $p(e^{\mathbf{z}})$
7. $\check{\mathbf{x}} \leftarrow$ L-BFGS-B $[-\alpha(\mathbf{x})]$
8. **if** $\alpha(\check{\mathbf{x}}) > \tilde{\alpha}$ **then**
9. $\tilde{\alpha} \leftarrow \alpha(\check{\mathbf{x}})$
10. $\mathbf{x}_t \leftarrow \check{\mathbf{x}}$

Part B: q-Expected Improvement

11. **for** $i = 1$ to N_{restart} **do**
12. $\mathbf{x} \leftarrow$ Draw sample from $p(e^{\mathbf{z}})$
13. **for** $j = 1$ to q **do**
14. $\check{\mathbf{x}} \leftarrow$ L-BFGS-B $[-\alpha(\mathbf{x})]$
15. $\text{col}_j[\tilde{\mathbf{X}}] \leftarrow \check{\mathbf{x}}$
16. $\mathbf{x} \leftarrow \check{\mathbf{x}}$
17. **if** $\alpha(\text{col}_{N_{\text{restart}}}[\tilde{\mathbf{X}}]) > \tilde{\alpha}$ **then**
18. $\tilde{\alpha} \leftarrow \alpha(\text{col}_{N_{\text{restart}}}[\tilde{\mathbf{X}}])$
19. $\mathbf{X}_t \leftarrow \tilde{\mathbf{X}}$

Eq. (37). The q resulting values of EI are averaged, giving qEI for the q -batch,

$$qEI(\mathbf{X}) = \mathbb{E}\left[\max_{i=1,\dots,q} (\mu(\mathbf{x}_i) + \sigma(\mathbf{x}_i)z - f', 0)\right] \quad (38)$$

$$\approx \frac{1}{q} \sum_{i=1}^q EI(\mathbf{x}_i). \quad (39)$$

Unlike the analytical acquisition function EI which yields only one candidate, qEI yields q candidates to be subsequently evaluated in parallel, modifying Eqs. (31) and (32) to

$$\mathbf{X}_t = \arg \max_{\mathbf{X}=[\mathbf{x}_1,\dots,\mathbf{x}_q]} \alpha(f(\mathbf{X})), \quad (40)$$

$$\mathcal{D}|_t = \mathcal{D}|_{t-1} \cup \{(\mathbf{X}_t, f(\mathbf{X}_t))\}. \quad (41)$$

qEI therefore samples the acquisition function and objective function spaces more rapidly than the analytical acquisition functions. However, as q increases, the optimization shifts from a Bayesian framework to a Monte Carlo framework. In this study, $q = 4$ was found to appropriately balance the benefits of sequential Bayesian optimization with the robustness of quasi-Monte Carlo sampling.

3. Acquisition function optimization

Exhaustively evaluating the acquisition function to solve Eq. (31) or Eq. (40) is computationally expensive for higher dimensional parameter spaces. In practice, an auxiliary optimization is performed to suggest samples for the next trial. Here again the L-BFGS-B algorithm is used,^{54,55} and as Eqs. (31) and (40) are maximization problems, the auxiliary optimization is transformed to a minimization problem by supplying the negated acquisition function as the objective function.

Since acquisition functions are often non-convex and can contain large regions with zero gradient, the auxiliary optimization is sensitive to the starting point. To improve performance, we rely on heuristics whereby the auxiliary optimization is performed using N_{restart} restarts. Starting points are chosen by first evaluating the acquisition function α at N_{raw} random points $\tilde{\mathbf{X}} \in \mathcal{X}$,

$$\tilde{\alpha} = \alpha(\tilde{\mathbf{X}}). \quad (42)$$

From these random evaluations of the acquisition function, a sample Z-distribution is computed,

$$\mathbf{z} = \frac{\tilde{\alpha} - \text{mean}(\tilde{\alpha})}{\text{std}(\tilde{\alpha})}, \quad (43)$$

which is used to construct an exponentiated distribution $p(e^{\mathbf{z}})$ from which N_{restart} starting points are drawn without replacement. The acquisition function's maximizer $\check{\mathbf{x}}$ is returned by L-BFGS-B for each of the N_{restart} starting points. The point $\check{\mathbf{x}}$ corresponding to the highest value of $\alpha(\check{\mathbf{x}})$ from

the N_{restart} restarts provides the next candidate point \mathbf{x}_t . Part A of [Algorithm 1](#) summarizes optimization of the EI acquisition function.

For each of the N_{restart} auxiliary optimizations for the quasi-Monte Carlo acquisition function qEI, q samples $\mathbf{X} = [\mathbf{x}_1, \dots, \mathbf{x}_q] \in \mathcal{X}$ are sequentially drawn from $p(\mathbf{e}^{\mathbf{z}})$. Each of the q samples serves as a starting point for maximizing the acquisition function by L-BFGS-B, and the maximizing points $\tilde{\mathbf{X}}$ are evaluated by the acquisition function. The maximizing points $\tilde{\mathbf{X}}$ corresponding to the highest value of $\alpha(\tilde{\mathbf{X}})$ from the N_{restart} restarts provides the next candidate points \mathbf{X}_t . Part B of [Algorithm 1](#) summarizes optimization of the qEI acquisition function.

D. Implementation

Implementation of Bayesian optimization with a GP surrogate model is shown in [Algorithm 2](#), and parameter values used are in Table I. First, N_{init} samples are drawn from the parameter space using a Sobol sequence²¹ and evaluated by the objective function. The initializing trials establish a reasonable prior distribution for the GP surrogate model. With the GP model fit, the Bayesian framework proceeds by optimizing the acquisition function α and generating candidate samples which are evaluated. Data from the new trials are appended to the existing data \mathcal{D} , and the GP model is fit with the updated data. This process repeats until the total number of trials N has been reached.

Bayesian optimization using the EI acquisition function is illustrated in Fig. 3 for one-dimensional range estimation for a simulated broadband source at 5.0 km; environment and array details are given in Sec. IV A. The GP is initialized with 8 trials sampled by a Sobol sequence. GP fit to the data is poor in early iterations but improves as observations are added. The acquisition function adaptively balances

ALGORITHM 2. Bayesian optimization with GP surrogate model.

Input: Parameter domain \mathcal{X} , objective function f , kernel function \mathcal{K} , acquisition function α , warmup evaluations N_{init} , total evaluations N

Output: Best estimate of parameters $\hat{\mathbf{x}}$

Initialization:

1. $f' \leftarrow 0, \theta \leftarrow \mathbb{R}$
2. **for** $t = 1$ **to** N_{init} **do**
3. $\mathbf{x}_t \leftarrow \text{SOBOL}[\mathcal{X}]$ [Ref. 21]
4. $f_t \leftarrow f(\mathbf{x}_t)$ [Eq. (5)]
5. **if** $f_t > f'$ **then**
6. $\hat{\mathbf{x}} \leftarrow \mathbf{x}_t, f' \leftarrow f_t$

Optimization:

7. **for** $t = N_{\text{init}} + 1$ **to** N **do**
8. $\mu \leftarrow \mathbb{E}[f(\mathbf{X})]$ [Eq. (7)]
9. $\theta \leftarrow \text{L-BFGS-B } [\mathcal{K}(\mathbf{X}, \mathbf{X}; \theta)]$ [Sec. III B 2]
10. $\Sigma \leftarrow \mathcal{K}(\mathbf{X}, \mathbf{X}; \theta)$ [Eq. (9)]
11. $\mathcal{GP} \leftarrow \mathcal{N}(\mu, \Sigma)$ [Eq. (10)]
12. $\mathbf{x}_t \leftarrow \arg \max_{\mathbf{x}} \alpha(\mathbf{x})$ [[Algorithm 1](#)]
13. $f_t \leftarrow f(\mathbf{x}_t)$
14. **if** $f_t > f'$ **then**
15. $\hat{\mathbf{x}} \leftarrow \mathbf{x}_t, f' \leftarrow f_t$

TABLE I. Bayesian optimization strategy parameters.

| Parameter | Description | Value |
|----------------------|--|-------|
| N | Total trials | 144 |
| N_{init} | Warm-up trials | 128 |
| N_{restart} | Acquisition function re-starts | 40 |
| N_{raw} | Raw samples for acquisition function optimization [Alg. 1] | 1024 |
| q | Batch size for q-Expected Improvement | 4 |

exploitation and exploration, with maximum values alternating between areas of high uncertainty (exploration) and areas with large objective function values (exploitation). The optimal solution is generally located by the 5th trial; in later trials, the acquisition function shape approaches a delta function, indicating a high confidence in the solution.

IV. RESULTS

Source localization is demonstrated using simulated and experimental data. A fixed budget of 144 trials is set for all optimization strategies. For the Bayesian strategies, the GP prior distribution is initialized with 128 trials sampled by a Sobol sequence. Two Bayesian strategies are evaluated:

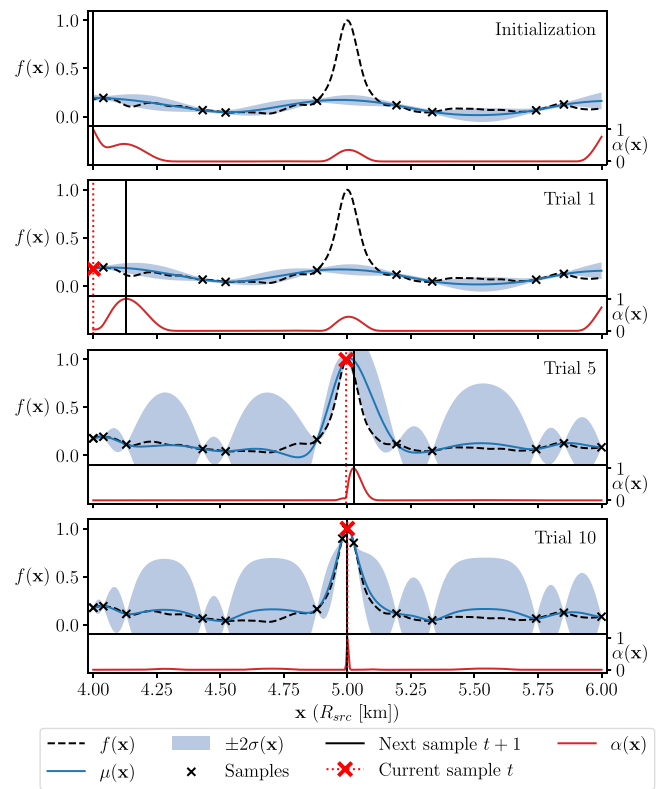


FIG. 3. (Color online) Range estimation for a simulated broadband source at 60 m depth and 5 km range using Bayesian optimization with GP surrogate model. Optimization is initialized with eight quasi-random samples. Top panels show the true objective function $f(\mathbf{x})$ (black dashed), and the mean function (blue) and standard error (blue shaded) of the GP. Bottom panels show the normalized expected improvement acquisition function $\alpha(\mathbf{x})$ [Eq. (37)]. The maximum of the acquisition function (vertical solid line) guides the location of the subsequent trial.

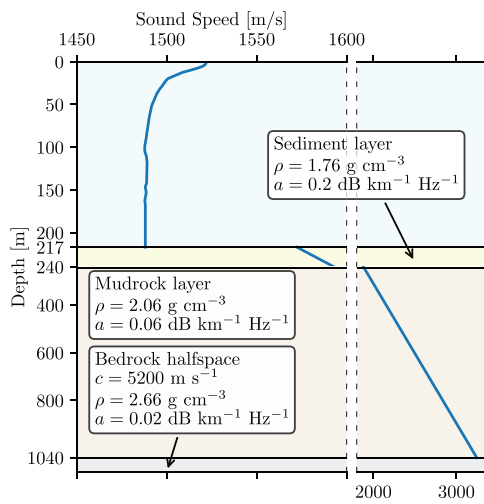


FIG. 4. (Color online) Sound speed profile and geoacoustic properties used for simulating acoustic propagation.

Sobol + GP/EI, which uses the EI acquisition function, and Sobol + GP/qEI, which uses the qEI acquisition function with $q=4$. For comparison, 144 trials of Sobol sequence sampling are evaluated, as well as 144 trials of grid search on an evenly spaced 12×12 grid.

A. Simulations

Measured data \mathbf{d} are simulated from the SWellEx-96 experiment.^{58,59} The environment, represented in Fig. 4, comprises a shallow, downward-refracting waveguide. A vertical line array (VLA) of 64 hydrophones evenly spaced between depths of 94.125 and 212.5 m (1.875 m spacing) recorded signals from an acoustic source towed by RV *Sprout* at a depth of approximately 60 m. The measured

acoustic field \mathbf{d} and replica fields \mathbf{d}^* are computed using the KRAKEN normal mode propagation model.⁶⁰ The source is simulated transmitting at $\Omega = \{148, 166, 201, 235, 283, 338, 388\}$ Hz from depth $z_{src} = 60$ m at ranges $R_{src} = \{1.0, 3.0, 5.0, 7.0\}$ km. The range search space is a ± 1 km window centered around the simulated source ranges R_{src} . For $R_{src} = 1.0$ km, the range search space is 1.01 ± 1 km to avoid near field effects. The depth search space is 60 ± 40 m. Because the Bayesian and Sobol sequence strategies are quasi-random, 100 Monte Carlo simulations are performed to assess performance.

Figure 5 shows localization results for each optimization strategy, with each row corresponding to a simulated source range. The two-dimensional broadband ambiguity surface of Eq. (5) is shown in the left column and constitutes the objective function $f(\mathbf{x})$ modeled by the GP surrogate model. In all cases, Sobol + GP/EI and Sobol + GP/qEI outperform Sobol sampling and grid search according to the best observed objective function value \hat{f} , range error, and depth error. This is due to the grid search evaluating local optima. Grid search performance is noteworthy in that, though \hat{f} increases as the grid is evaluated, the apparent improvement might not give a decrease in range and depth errors.

Though fitting the GP surrogate model and optimizing the acquisition function are somewhat computationally expensive, on average the Bayesian strategies converge on the global optimum in far fewer trials than the Sobol sequence and grid search strategies alone. Figure 6 shows traces of \hat{f} as a function of run time for the 100 Monte Carlo runs of each strategy. Run times were measured one run at a time on a 16-core laptop computer. The Bayesian strategies ran for 144 trials (128 Sobol, 16 Bayesian), while the Sobol sequence and grid search strategies ran for 1024 trials. More trials and time are required for Sobol sampling and grid

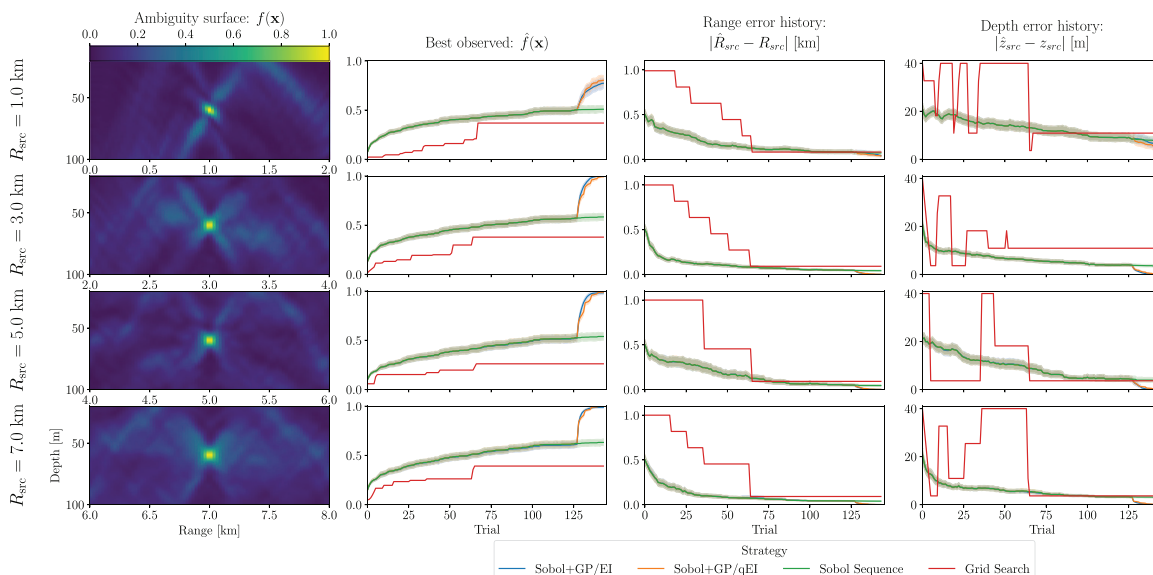


FIG. 5. (Color online) Two-dimensional matched field processing (MFP) multi-frequency ambiguity surfaces (left column) for a simulated source at 60 m depth and 1, 3, 5, 7 km range. Best observed optimization performance (middle-left column), source range error (middle-right column), and source depth error (right column) from 100 Monte Carlo simulations are shown for each trial. Solid colored lines indicate mean values and shaded regions indicate standard deviation.

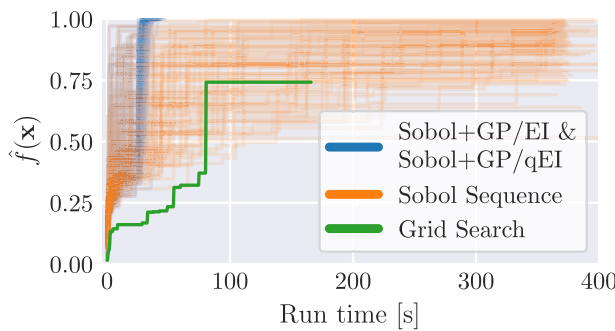


FIG. 6. (Color online) Highest observed objective vs run time using a simulated source at $R_{\text{src}} = 3.0 \text{ km}$ and $z_{\text{src}} = 60 \text{ m}$. Sobol + GP/EI and Sobol + GP/qEI (blue) consist of 128 Sobol sequence trials followed by 16 GP/EI or GP/qEI steps (144 total trials); Sobol sequence (orange) of 1024 trials; and grid search (green) of a 32×32 grid (1024 trials).

search to converge on the global optimum than for the Bayesian strategies.

B. Experimental data

The following analysis uses SWellEx-96 experimental data recorded during event S5, conducted between 23:15 and 00:30 GMT on 10–11 May 1996 12 km west of Point Loma, California.^{58,59} RV *Sprout* towed an acoustic source along an isobath of 200 m, though actual depth varied, with the source tow commencing in 220 m of water and the second half of the tow occurring in 180 m of water. RV *Sprout* proceeded from south to north at 5 knots (2.5 m/s), with a closest point of approach (CPA) to the VLA of 900 m. The source was towed at 60 m depth and transmitted five sets of tonals with varying source levels. Data were recorded by the VLA with a 1500-Hz sampling rate. The 64-element array is described in Sec. IV A.

Data between 23:21 and 00:24 GMT were processed in 350 non-overlapping time steps. At the starting point, halfway point, and CPA of the source tow, the deep source ceased broadcasting CW tonals and transmitted frequency-modulated (FM) chirps; these time segments are omitted.

Replica vectors \mathbf{d}^* are calculated at each frequency in $\Omega = \{148, 166, 201, 235, 283, 338, 388\} \text{ Hz}$ using the

environmental model in Fig. 4. These frequencies correspond to the upper seven tonals from the loudest set transmitted by the source. To approximate array tilt and improve localization, a 1° tilt away from the source is applied to replica vector calculations at all time steps.⁵⁹ Measurement vectors \mathbf{d} are obtained from the discrete Fourier transform of the experimental data at each time step and at the frequencies in Ω .

The range search space is a $\pm 1 \text{ km}$ window centered around the GPS position of RV *Sprout* (R_{GPS}) at each time step. When $R_{\text{GPS}} < 1.01 \text{ km}$, the range search space is $1.01 \pm 1 \text{ km}$ to avoid near field effects; when $R_{\text{GPS}} > 7.0 \text{ km}$, the search space is $7.0 \pm 1 \text{ km}$. The depth search space is $60 \pm 40 \text{ m}$.

High-resolution MFP (200 range bins, 100 depth bins) establishes a baseline against which to compare optimization strategies and compute localization error. Results from high-resolution MFP are plotted in the upper left panel of Fig. 7 for each time step. As RV *Sprout* approaches the array, the ship's GPS range is closer than the high-resolution MFP estimate due to the scope of the cable towing the source; at CPA, the disparity expectedly reverses. Over the course of the source tow, the high-resolution MFP depth estimate indicates a gradual depth change from 50 to 70 m. The apparent depth change results from a mirage effect arising from mismatch between true and modeled (217 m) bathymetry used to compute replica vectors \mathbf{d}^* .⁶¹

Range and depth estimation are performed using the Sobol + GP/EI and Sobol + GP/qEI Bayesian optimization strategies, and the grid search and Sobol sampling as described in Sec. IV A. For additional comparison, results from SBL^{26–29,62} computed at the same points as the grid search are presented. No prior information is passed from one time step to the next, and the optimizations are reinitialized at each time step. Figure 7 shows results of range and depth estimation at each time step for all strategies, and Fig. 8 shows the range and depth estimation errors relative to high-resolution MFP. All methods localize the source reasonably well, but the Bayesian methods are able to track the source more closely than grid search and Sobol sampling. At longer ranges, Bayesian methods track the source more

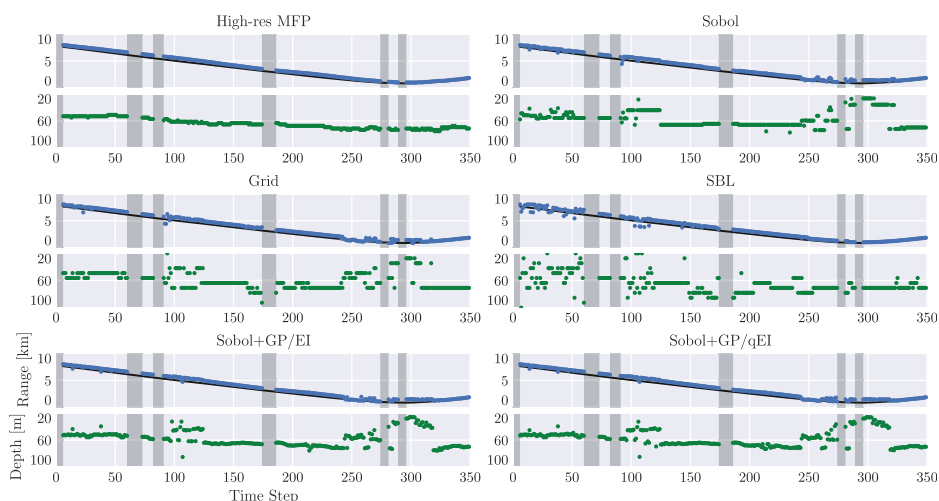


FIG. 7. (Color online) Range (blue) and depth (green) estimated localization for high-resolution matched field processing (MFP), low-resolution MFP (grid search), sparse Bayesian learning grid search (SBL), Sobol sampling, and Bayesian optimization using expected improvement (Sobol + GP/EI) and quasi-Monte Carlo expected improvement (Sobol + GP/qEI) acquisition functions. The black line indicates the GPS range of RV *Sprout* to the array. Gray shaded areas indicate when the source stopped transmitting.

closely than SBL, whereas at close range, SBL out-performs the Bayesian methods. The mean absolute and median absolute errors over the entire source tow are listed for each strategy in Table II. Except for SBL, performance suffers when the source is near CPA, likely due to the complicated structure of the ambiguity surface at this range: from Fig. 5, the ambiguity surface at $R_{\text{src}} = 1.0 \text{ km}$ has local optima in close proximity to the global optimum.

Figure 9 compares the GP mean and standard error surfaces to the objective function surface upon completion of the Sobol + GP/EI strategy for time step 200. In the region surrounding the global optimum where sampling is most dense, the mean function $\mu(\mathbf{x})$ resembles the objective function $f(\mathbf{x})$ and has low variance.

V. DISCUSSION

We find the success of the Sobol + GP/EI and Sobol + GP/qEI strategies rests on establishing a reasonable prior over the objective function prior to commencing Bayesian optimization. Two primary factors contribute to this prior: the domain of the parameter space and the number of warm-up trials.

The complicated structure of the ambiguity surface informed our choice of a parameter space constrained to 2 km range and 80 m depth windows. When a broader search space is used (e.g., 1 to 10 km range and 0 to 200 m depth), there are more local optima in the parameter space and Bayesian optimization converges on the optimal solution less reliably. This can be mitigated by using more warm-up trials to obtain a better prior.

The appropriate balance between warm-up trials and Bayesian optimization trials is a design consideration which must be evaluated according to the data, objective function, parameter space, and computational budget available. We arrived at a ratio of 128 warm-up trials to 16 Bayesian optimization trials through experimentation. Initial attempts to invert the ratio resulted in a poor prior, and Bayesian optimization was unable to reliably converge on a solution due to the complicated structure of the objective function. Since Bayesian optimization trials take approximately 1 s to fit the GP and optimize the acquisition function, using 16 warm-up trials and 128 Bayesian trials not only resulted in poor convergence but also expended more computation time. The ratio of warm-up trials to Bayesian optimization trials is therefore best evaluated against the expected number of optima in the objective function, which is itself dependent on the domain of the parameter space.

Experimentation with adjusting the size of the parameter space and the ratio of warm-up trials to Bayesian optimization trials suggest our method is better suited for applications where there is a strong prior over range and depth rather than for wide-area search. Cases where the approximate location of a source is known but precise localization is required could include localization of towed sources, underwater vehicles, and oceanographic moorings.

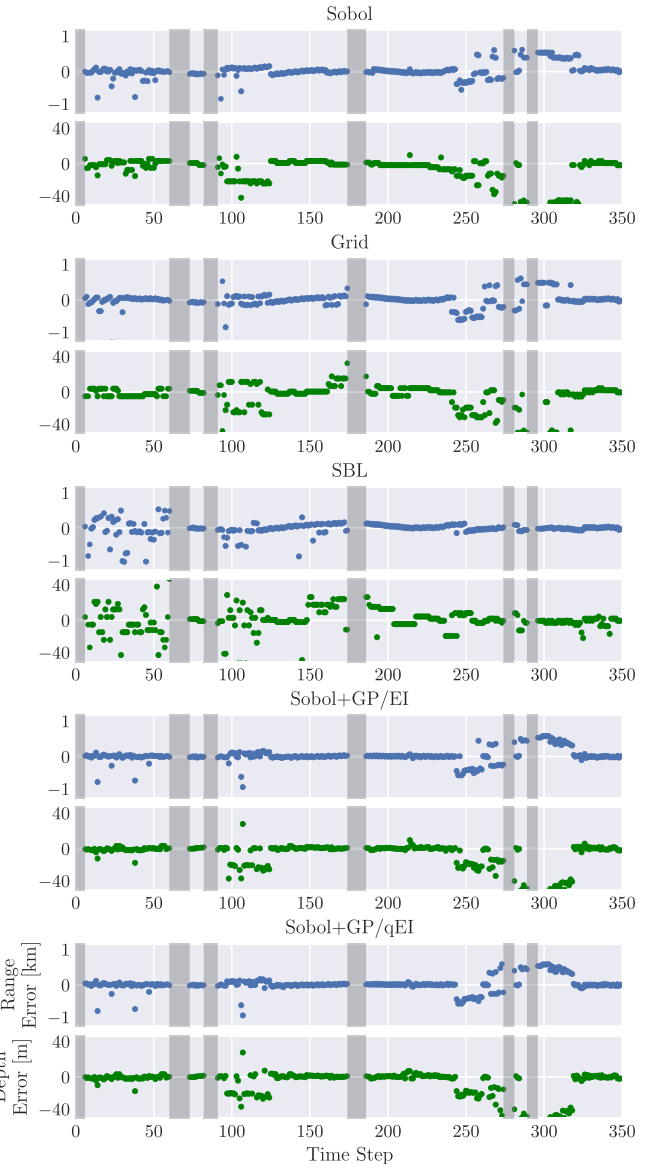


FIG. 8. (Color online) Range (blue) and depth (green) estimation errors relative to high-resolution matched field processing. Gray shaded areas indicate when the source stopped transmitting.

An important consideration for this method is that the quality of the optimization is contingent on the quality of the ambiguity surface. If the signal-to-noise ratio of the data is low, a sidelobe could be the global optimum rather than

TABLE II. Mean absolute error (MAE) and median absolute error (Med AE) with respect to high-resolution matched field processing.

| Strategy | Range [km] | | Depth [m] | |
|----------------------|--------------|--------------|--------------|--------------|
| | MAE | Med AE | MAE | Med AE |
| Grid | 0.111 | 0.046 | 7.795 | 3.576 |
| SBL | 0.130 | 0.048 | 7.500 | 3.697 |
| Sobol | 0.107 | 0.041 | 8.308 | 2.543 |
| Sobol + GP/EI | 0.090 | 0.017 | 7.125 | 0.974 |
| Sobol + GP/qEI | 0.093 | 0.017 | 7.477 | 1.286 |

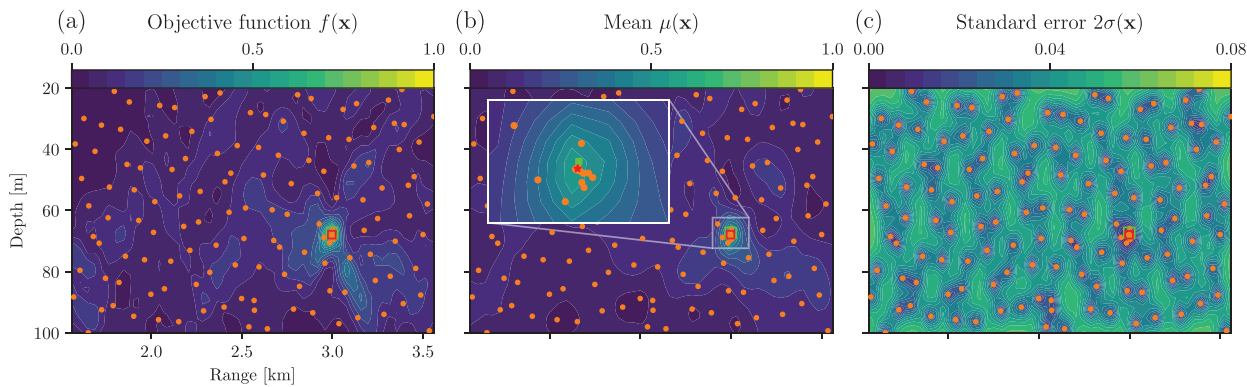


FIG. 9. (Color online) (a) Objective function (ambiguity surface), (b) mean function, and (c) standard error surface for the GP posterior at time step 200 ($R_{\text{GPS}} = 2.56 \text{ km}$). Optimization was performed using the EI acquisition function. Samples (orange circles) and the actual (green) and estimated (red) source positions are indicated. The inset in (b) shows the dense sampling pattern and best estimate from Bayesian optimization converging on the global optimum.

the peak corresponding to the true source location. Adequate signal processing steps must therefore be taken to maximize signal gain and reduce sidelobes. Approaches for reducing sidelobes employ high-resolution beamformers such as SBL^{26–29} or multiple signal classification (MUSIC)²⁵ as the objective function. However, in optimization applications, conventional beamforming is often preferred as it has broad peaks and is more robust.

VI. CONCLUSION

We have demonstrated efficient and accurate source localization with sequential Bayesian optimization when the ambiguity surface is modeled as a Gaussian process and sampling is guided by a probabilistic acquisition function. In addition to being sample-efficient, the Sobol + GP/EI and Sobol + GP/qEI strategies are advantageous as they are suitable for non-convex objective functions and require no information about the gradient of the objective function.

Simulations of a shallow-water waveguide and real data from an acoustic source tow experiment demonstrated that the Sobol + GP/EI and Sobol + GP/qEI strategies converge on the global optimum rapidly and yield superior results compared to grid search and quasi-random sampling strategies. We conclude the Sobol + GP/EI and Sobol + GP/qEI strategies are best employed as a hybrid sampling strategy in which the majority of trials in a fixed budget establish the prior over the objective, and the remaining Bayesian optimization trials fine-tune the optimization.

ACKNOWLEDGMENTS

This research was supported by the Office of Naval Research through Grant No. N00014-21-1-2267 and the National Defense Science and Engineering Graduate Fellowship for Jenkins. Code implementation of this research uses the GPyTorch,⁶³ BoTorch,¹⁵ and Adaptive Experimentation Platform⁶⁴ libraries. SBL was implemented with the SBL4 package.⁶²

¹C. E. Rasmussen and C. K. I. Williams, *Gaussian Processes for Machine Learning* (MIT Press, Cambridge, MA, 2006).

²D. Caviedes-Nozal, N. A. B. Riis, F. M. Heuchel, J. Brunskog, P. Gerstoft, and E. Fernandez-Grande, “Gaussian processes for sound field reconstruction,” *J. Acoust. Soc. Am.* **149**(2), 1107–1119 (2021).

³Z.-H. Michalopoulou, P. Gerstoft, and D. Caviedes-Nozal, “Matched field source localization with Gaussian processes,” *JASA Express Lett.* **1**(6), 064801 (2021).

⁴Z.-H. Michalopoulou and P. Gerstoft, “Inversion in an uncertain ocean using Gaussian processes,” *J. Acoust. Soc. Am.* **153**(3), 1600–1611 (2023).

⁵I. D. Khurjekar, P. Gerstoft, C. F. Mecklenbräuker, and Z.-H. Michalopoulou, “Direction-of-arrival estimation using Gaussian process interpolation,” in *Proceedings of International Conference on Acoustics, Speech and Signal Processing* (2023), pp. 1–5.

⁶D. Zimmerman, C. Pavlik, A. Ruggles, and M. P. Armstrong, “An experimental comparison of ordinary and universal kriging and inverse distance weighting,” *Math. Geol.* **31**(4), 375–390 (1999).

⁷K. P. Murphy, *Probabilistic Machine Learning: An Introduction* (MIT Press, Cambridge, MA, 2022).

⁸B. Shahriari, K. Swersky, Z. Wang, R. P. Adams, and N. de Freitas, “Taking the human out of the loop: A review of Bayesian optimization,” *Proc. IEEE* **104**(1), 148–175 (2016).

⁹J. J. Beland and P. B. Nair, “Bayesian optimization under uncertainty,” in *NIPS BayesOpt 2017 Workshop*, Long Beach, CA (2017), Vol. 3.

¹⁰D. R. Jones, “A taxonomy of global optimization methods based on response surfaces,” *J. Global Optim.* **21**(4), 345–383 (2001).

¹¹N. Srinivas, A. Krause, S. M. Kakade, and M. W. Seeger, “Information-theoretic regret bounds for Gaussian process optimization in the bandit setting,” *IEEE Trans. Inf. Theory* **58**(5), 3250–3265 (2012).

¹²D. Ginsbourger, R. Le Riche, and L. Carraro, “Kriging is well-suited to parallelize optimization,” in *Computational Intelligence in Expensive Optimization Problems* (Springer, Berlin, Heidelberg) (2010), Vol. 2, pp. 131–162.

¹³J. T. Wilson, F. Hutter, and M. P. Deisenroth, “Maximizing acquisition functions for Bayesian optimization,” *Adv. Neural Inf. Process. Syst.* (published online 2018), [arXiv:1805.10196](https://arxiv.org/abs/1805.10196).

¹⁴J. Wang, S. C. Clark, E. Liu, and P. I. Frazier, “Parallel Bayesian global optimization of expensive functions,” *Oper. Res.* **68**(6), 1850–1865 (2020).

¹⁵M. Balandat, B. Karrer, D. R. Jiang, S. Daulton, B. Letham, A. G. Wilson, and E. Bakshy, “BoTorch: A framework for efficient Monte-Carlo Bayesian optimization,” *Adv. Neural Inf. Process. Syst.* **33**, 21524–21538 (2020).

¹⁶W. Jenkins, P. Gerstoft, and Y. Park, “Bayesian optimization with Gaussian process surrogate model for geoacoustic inversion and parameter estimation,” <https://github.com/NeptuneProjects/BOGP> (2023) (Last viewed July 25, 2023).

¹⁷A. Baggeroer, W. Kuperman, and P. Mikhalevsky, “An overview of matched field methods in ocean acoustics,” *J. Ocean. Eng.* **18**(4), 401–424 (1993).

¹⁸J. Bergstra and Y. Bengio, “Random search for hyper-parameter optimization,” *J. Mach. Learn. Res.* **13**(10), 281–305 (2012).

- ¹⁹I. Sobol', "On the distribution of points in a cube and the approximate evaluation of integrals," *USSR Comp. Math. Math. Phys.* **7**(4), 86–112 (1967).
- ²⁰A. Saltelli, M. Ratto, T. Andres, F. Campolongo, J. Cariboni, D. Gatelli, M. Saisana, and S. Tarantola, *Global Sensitivity Analysis. The Primer*, 1st ed. (Wiley, West Sussex, UK, 2007).
- ²¹S. Joe and F. Y. Kuo, "Constructing Sobol sequences with better two-dimensional projections," *SIAM J. Sci. Comput.* **30**(5), 2635–2654 (2008).
- ²²L. Dumaz, J. Garnier, and G. Lepoulter, "Acoustic and geoacoustic inverse problems in randomly perturbed shallow-water environments," *J. Acoust. Soc. Am.* **146**(1), 458–469 (2019).
- ²³B. Kayser, B. Gauvreau, D. Écotière, and V. Mallet, "Wind turbine noise uncertainty quantification for downwind conditions using metamodeling," *J. Acoust. Soc. Am.* **151**(1), 390–401 (2022).
- ²⁴J. Nocedal and S. J. Wright, *Numerical Optimization*, Springer Series in Operations Research, 2nd ed. (Springer, New York, 2006).
- ²⁵R. Schmidt, "Multiple emitter location and signal parameter estimation," *IEEE Trans. Antennas Propag.* **34**(3), 276–280 (1986).
- ²⁶M. E. Tipping, "Sparse Bayesian learning and the relevance vector machine," *J. Mach. Learn. Res.* **1**, 211–244 (2001).
- ²⁷D. Wipf and B. Rao, "Sparse Bayesian learning for basis selection," *IEEE Trans. Signal Process.* **52**(8), 2153–2164 (2004).
- ²⁸K. L. Gemba, S. Nannuru, P. Gerstoft, and W. S. Hodgkiss, "Multi-frequency sparse Bayesian learning for robust matched field processing," *J. Acoust. Soc. Am.* **141**(5), 3411–3420 (2017).
- ²⁹Y. Park, F. Meyer, and P. Gerstoft, "Sequential sparse Bayesian learning for time-varying direction of arrival," *J. Acoust. Soc. Am.* **149**(3), 2089–2099 (2021).
- ³⁰Y. Chi, Y. M. Lu, and Y. Chen, "Nonconvex optimization meets low-rank matrix factorization: An overview," *IEEE Trans. Signal Process.* **67**(20), 5239–5269 (2019).
- ³¹S. Li, L. Cheng, T. Zhang, H. Zhao, and J. Li, "Graph-guided Bayesian matrix completion for ocean sound speed field reconstruction," *J. Acoust. Soc. Am.* **153**(1), 689–710 (2023).
- ³²M. J. Bianco, P. Gerstoft, J. Traer, E. Ozanich, M. A. Roch, S. Gannot, and C.-A. Deledalle, "Machine learning in acoustics: Theory and applications," *J. Acoust. Soc. Am.* **146**(5), 3590–3628 (2019).
- ³³Y. Liu, H. Niu, and Z. Li, "A multi-task learning convolutional neural network for source localization in deep ocean," *J. Acoust. Soc. Am.* **148**(2), 873–883 (2020).
- ³⁴P.-A. Grumiaux, S. Kitić, L. Girin, and A. Guérin, "A survey of sound source localization with deep learning methods," *J. Acoust. Soc. Am.* **152**(1), 107–151 (2022).
- ³⁵A. Varon, J. Mars, and J. Bonnel, "Approximation of modal wavenumbers and group speeds in an oceanic waveguide using a neural network," *JASA Express Lett.* **3**(6), 066003 (2023).
- ³⁶L. Zhang, T. Zhang, H.-S. Shin, and X. Xu, "Efficient underwater acoustic localization method based on time difference and bearing measurements," *IEEE Trans. Instrum. Meas.* **70**, 1–16 (2021).
- ³⁷P. Gerstoft, "Inversion of seismooceanic data using genetic algorithms and *a posteriori* probability distributions," *J. Acoust. Soc. Am.* **95**(2), 770–782 (1994).
- ³⁸P. Gerstoft and C. F. Mecklenbräuker, "Ocean acoustic inversion with estimation of *a posteriori* probability distributions," *J. Acoust. Soc. Am.* **104**(2), 808–819 (1998).
- ³⁹S. E. Dosso, "Quantifying uncertainty in geoacoustic inversion. I. A fast Gibbs sampler approach," *J. Acoust. Soc. Am.* **111**(1), 129–142 (2002).
- ⁴⁰S. E. Dosso and P. L. Nielsen, "Quantifying uncertainty in geoacoustic inversion. II. Application to broadband, shallow-water data," *J. Acoust. Soc. Am.* **111**(1), 143–159 (2002).
- ⁴¹S. E. Dosso and M. J. Wilmut, "Uncertainty estimation in simultaneous Bayesian tracking and environmental inversion," *J. Acoust. Soc. Am.* **124**(1), 82–97 (2008).
- ⁴²M. D. Collins, W. A. Kuperman, and H. Schmidt, "Nonlinear inversion for ocean-bottom properties," *J. Acoust. Soc. Am.* **92**(5), 2770–2783 (1992).
- ⁴³M. D. Collins, W. A. Kuperman, and W. L. Siegmann, "Propagation and inversion in complex ocean environments," in *Full Field Inversion Methods in Ocean and Seismo-Acoustics* (Kluwer Academic, The Netherlands, 1995), pp. 15–20.
- ⁴⁴M. D. Collins and L. Fishman, "Efficient navigation of parameter landscapes," *J. Acoust. Soc. Am.* **98**(3), 1637–1644 (1995).
- ⁴⁵J. Dettmer, S. E. Dosso, and C. W. Holland, "Trans-dimensional geoacoustic inversion," *J. Acoust. Soc. Am.* **128**(6), 3393–3405 (2010).
- ⁴⁶J. Dettmer and S. E. Dosso, "Trans-dimensional matched-field geoacoustic inversion with hierarchical error models and interacting Markov chains," *J. Acoust. Soc. Am.* **132**(4), 2239–2250 (2012).
- ⁴⁷S. E. Dosso and J. Bonnel, "Joint trans-dimensional inversion for water-column sound speed and seabed geoacoustic models," *JASA Express Lett.* **3**(6), 060801 (2023).
- ⁴⁸P. Gerstoft, "Inversion of acoustic data using a combination of genetic algorithms and the Gauss–Newton approach," *J. Acoust. Soc. Am.* **97**(4), 2181–2190 (1995).
- ⁴⁹M. R. Fallat and S. E. Dosso, "Geoacoustic inversion via local, global, and hybrid algorithms," *J. Acoust. Soc. Am.* **105**(6), 3219–3230 (1999).
- ⁵⁰N. Booth, P. Baxley, J. Rice, P. Schey, W. Hodgkiss, G. D'Spain, and J. Murray, "Source localization with broad-band matched-field processing in shallow water," *J. Ocean. Eng.* **21**(4), 402–412 (1996).
- ⁵¹Z.-H. Michalopoulou and M. Porter, "Matched-field processing for broad-band source localization," *J. Ocean. Eng.* **21**(4), 384–392 (1996).
- ⁵²R. M. Neal, *Bayesian Learning for Neural Networks*, Lecture Notes in Statistics Vol. 118 (Springer, New York, 1996).
- ⁵³K. P. Murphy, *Probabilistic Machine Learning: Advanced Topics* (MIT Press, Cambridge, MA, 2023).
- ⁵⁴R. H. Byrd, P. Lu, J. Nocedal, and C. Zhu, "A limited memory algorithm for bound constrained optimization," *SIAM J. Sci. Comput.* **16**(5), 1190–1208 (1995).
- ⁵⁵C. Zhu, R. H. Byrd, P. Lu, and J. Nocedal, "Algorithm 778: L-BFGS-B: Fortran subroutines for large-scale bound-constrained optimization," *ACM Trans. Math. Software* **23**(4), 550–560 (1997).
- ⁵⁶S. Kim, G. F. Edelmann, W. A. Kuperman, W. S. Hodgkiss, H. C. Song, and T. Akal, "Spatial resolution of time-reversal arrays in shallow water," *J. Acoust. Soc. Am.* **110**(2), 820–829 (2001).
- ⁵⁷B. Letham, B. Karre, G. Ottone, and E. Bakshy, "Constrained Bayesian optimization with noisy experiments," [arXiv:1706.07094](https://arxiv.org/abs/1706.07094) (2018).
- ⁵⁸R. T. Bachman, P. W. Schey, N. O. Booth, and F. J. Ryan, "Geoacoustic databases for matched-field processing: Preliminary results in shallow water off San Diego, California," *J. Acoust. Soc. Am.* **99**(4), 2077–2085 (1996).
- ⁵⁹Marine Physical Laboratory, "SWellEx-96 Experiment," <http://swellex96.ucsd.edu/> (2003) (Last viewed May 30, 2023).
- ⁶⁰M. B. Porter, "The KRAKEN normal mode program," SACLANT Undersea Research Centre Memorandum (SM-245)/Naval Research Laboratory Memorandum Report 6920 (1991).
- ⁶¹G. L. D'Spain, J. J. Murray, and W. S. Hodgkiss, "Mirages in shallow water matched field processing," *J. Acoust. Soc. Am.* **105**(6), 3245–3265 (1999).
- ⁶²Y. Park, S. Nannuru, K. Gemba, and P. Gerstoft, "SBL4 from NoiseLab," <https://github.com/gerstoft/SBL> (2020) (Last viewed May 30, 2023).
- ⁶³J. R. Gardner, G. Pleiss, D. Bindel, K. Q. Weinberger, and A. G. Wilson, "GPyTorch: Blackbox Matrix-Matrix Gaussian Process Inference with GPU Acceleration," *Adv. Neural Inf. Process. Syst.* (published online 2018), [arXiv:1809.11165](https://arxiv.org/abs/1809.11165).
- ⁶⁴Meta Platforms, Inc., "Adaptive Experimentation Platform," <https://ax.dev> (2023) (Last viewed May 30, 2023).